RSC Advances

PAPER

View Article Online
View Journal | View Issue

Cite this: *RSC Adv.*, 2024, **14**, 14126

Characterization and antitumor effect of doxorubicin-loaded Fe_3O_4–Au nanocomposite synthesized by electron beam evaporation for magnetic nanotheranostics

Valerii B. Orel, *[ab] Yurii A. Kurapov, [c] Stanislav Ye. Lytvyn, [c] Valerii E. Orel, [ab] Olexander Yu. Galkin, [b] Olga Yo. Dasyukevich, [a] Oleksandr Yu. Rykhalskyi, [a] Anatolii G. Diedkov, [a] Vasyl V. Ostafiichuk, [a] Sergii A. Lyalkin, [a] Anatoliy P. Burlaka, [d] Sergii V. Virko, [de] Mykola A. Skoryk, [f] Viacheslav V. Zagorodnii, [bf] Yaroslav A. Stelmakh, [c] Gennadii G. Didikin, [c] Olena I. Oranska, [g] Lucio Calcagnile, [h] Daniela E. Manno, [h] Rosaria Rinaldi [h] and Yana V. Nedostup [i]

Magnetic nanocomposites (MNC) are promising theranostic platforms with tunable physicochemical properties allowing for remote drug delivery and multimodal imaging. Here, we developed doxorubicin-loaded Fe_3O_4–Au MNC (DOX-MNC) using electron beam physical vapor deposition (EB-PVD) in combination with magneto-mechanochemical synthesis to assess their antitumor effect on Walker-256 carcinosarcoma under the influence of a constant magnetic (CMF) and electromagnetic field (EMF) by comparing tumor growth kinetics, magnetic resonance imaging (MRI) scans and electron spin resonance (ESR) spectra. Transmission (TEM) and scanning electron microscopy (SEM) confirmed the formation of spherical magnetite nanoparticles with a discontinuous gold coating that did not significantly affect the ferromagnetic properties of MNC, as measured by vibrating-sample magnetometry (VSM). Tumor-bearing animals were divided into the control (no treatment), conventional doxorubicin (DOX), DOX-MNC and DOX-MNC + CMF + EMF groups. DOX-MNC + CMF + EMF resulted in 14% and 16% inhibition of tumor growth kinetics as compared with DOX and DOX-MNC, respectively. MRI visualization showed more substantial tumor necrotic changes after the combined treatment. Quantitative analysis of T_2-weighted (T_2W) images revealed the lowest value of skewness and a significant increase in tumor intensity in response to DOX-MNC + CMF + EMF as compared with the control (1.4 times), DOX (1.6 times) and DOX-MNC (1.8 times) groups. In addition, the lowest level of nitric oxide determined by ESR was found in DOX-MNC + CMF + EMF tumors, which was close to that of the muscle tissue in the contralateral limb. We propose that the reason for the relationship between the observed changes in MRI and ESR is the hyperfine interaction of nuclear and electron spins in mitochondria, as a source of free radical production. Therefore, these results point to the use of EB-PVD and magneto-mechanochemically synthesized Fe_3O_4–Au MNC loaded with DOX as a potential candidate for cancer magnetic nanotheranostic applications.

Received 7th March 2024
Accepted 23rd April 2024

DOI: 10.1039/d4ra01777c

rsc.li/rsc-advances

1. Introduction

The unique physicochemical properties of magnetic nanoparticles have driven the application of nanotechnology for cancer diagnostics and treatment.[1,2] Recently, considerable effort has been directed to nanostructures synthesized from the combination of two or more different materials. This has the advantage of developing nanocomposites with tunable

[a]National Cancer Institute, Kyiv 03022, Ukraine. E-mail: orel.valeriy@gmail.com
[b]National Technical University of Ukraine "Igor Sikorsky Kyiv Polytechnic Institute", Kyiv 03056, Ukraine
[c]E.O. Paton Electric Welding Institute, Kyiv 03150, Ukraine
[d]R.E. Kavetsky Institute of Experimental Pathology, Oncology and Radiobiology, Kyiv 03022, Ukraine
[e]V.E. Lashkaryov Institute of Semiconductor Physics, Kyiv 03028, Ukraine
[f]G.V. Kurdyumov Institute for Metal Physics of the N.A.S. of Ukraine, Kyiv 03142, Ukraine
[g]Chuiko Institute of Surface Chemistry of the N.A.S. of Ukraine, Kyiv 03164, Ukraine
[h]University of Salento, Lecce 73100, Italy
[i]Taras Shevchenko National University of Kyiv, Kyiv 03680, Ukraine

characteristics distinct from their constituent materials. Magnetic nanocomposites (MNC) based on iron oxide, in particular magnetite (Fe_3O_4), are garnering great interest because of their use in drug delivery, magnetic resonance imaging (MRI) and magnetic hyperthermia. These have proven effective since such materials exhibit ferromagnetic or superparamagnetic properties and a large surface area to volume ratio.[3] Nonetheless, iron oxide nanostructures are prone to aggregate in a nonuniform manner upon interaction with the biological media, which may limit their biodistribution and even result in toxic side effects. One solution is to coat the surface of magnetite nanoparticles with another material, such as a noble metal or a polymer.[4,5] Gold represents an attractive material for enhancing the biocompatibility of MNC while maintaining the ability to initiate free radicals, including reactive oxygen (ROS) and nitrogen species (RNS).[6] Furthermore, the optical properties of gold can be used to promote plasmon-assisted free radical production by MNC under the influence of magnetic fields.[7,8]

It is important to begin with an understanding that mitochondria are one of the major sources of free radicals in mammalian cells due to proton-coupled electron transfer processes.[9] ROS generation is a widely accepted mechanism by which many anticancer drugs, such as doxorubicin (DOX), act on the tumor and its microenvironment. Drug-induced elevation in ROS levels leads to oxidative stress and cell damage.[10] Previous *in vitro* studies reported more pronounced antitumor effects of DOX-loaded Fe_3O_4–Au MNC (DOX-MNC) than that of free DOX.[11–13] Though conceptually simple, this approach alone is unable to target ROS and RNS formation at the tumor site and limit toxicity to normal tissues. The application of a constant magnetic field (CMF) offers the possibility of MNC delivery to the tumor, whereas a radiofrequency electromagnetic field (EMF) affects the kinetics of free radical reactions and subsequent ROS and RNS formation. It is immediately apparent that CMF not only aligns MNC with the field gradient but also exerts a magnetic force upon them. By applying mechanical stress on tumor cells in response to CMF, MNC alter mechanochemical transduction pathways involved in tumor development. A combination of MNC, CMF and EMF is of particular interest in the context of magneto-mechanochemical effects on proton-coupled electron transfer processes in mitochondria.[14] It has also been shown that DOX-MNC enhances the antitumor activity of the chemotherapeutic drug by modulating ROS production through the magneto-mechanochemical effects in the presence of CMF and EMF as well as improves tumor contrast in different imaging modalities.[15]

In practice, a straightforward way to fabricate MNC is by electron beam physical vapor deposition (EB-PVD) of iron in a porous NaCl matrix onto a substrate. NaCl solution is a choice of solvent for most chemotherapeutic agents. The effect of annealing or exposure to the oxygen atmosphere serves to oxidize iron embedded in the matrix.[16] EB-PVD is a technique in which molecule decomposition under electron irradiation forms nanostructures by the deposition of nonvolatile fragments on the substrate.[17,18] Given a uniform evaporation rate and distribution of vapor flows, this method does not lead to the formation of metal–ligand bonds, unlike chemical synthesis.[19] EB-PVD is also capable of engineering the surface functionality of iron oxide with coatings composed of a few nanometer-sized gold clusters.[20] However, the emission of electrons and ions during the procedure remains a serious challenge due to the unwanted shadow evaporation, cross-linking and bubble bursts associated with changes in the structure of MNC.[21]

In this study, we examine the physicochemical properties of magnetite-based MNC with gold coating (Fe_3O_4–Au) prepared using EB-PVD. Following magneto-mechanochemical synthesis, we then assess the tumor response to treatment with DOX-MNC under the influence of CMF and EMF by comparing Walker-256 carcinosarcoma growth kinetics, MRI scans and electron spin resonance (ESR) spectra.

2. Materials and methods

2.1 Synthesis of Fe_3O_4–Au MNC

The two steps in the synthesis of MNC by EB-PVD are the preparation of Fe_3O_4 nanoparticles followed by gold coating (Fig. 1).

Fe–NaCl nanostructures were deposited on a water-cooled copper substrate in the same vacuum step with a residual pressure of $\approx 10^{-2}$ Pa. Deposit morphology was controlled by evaporation rate, duration and substrate temperature, with iron nanoparticles embedded into a porous NaCl matrix. After the samples were soaked in a vacuum and bleeding air, they were detached from the substrate. Exposure to the atmosphere facilitated the oxidation of iron nanoparticles captured within the pores of the matrix material to magnetite. The resulting sample was refined, washed several times with distilled water and allowed to settle. Once Fe_3O_4 residue was collected and dried, we ground it using an agate mortar and repeated washing to remove NaCl.

Next, gold was vaporized by the electron beam in a reactor, where the vapors traveled through a chamber to magnetite nanoparticles placed in a water-cooled copper tank. The nanoparticles were thoroughly mixed while gold condensed to a solid phase on their surface.

2.2 Characterization of Fe_3O_4–Au MNC

MNC were analyzed at each step during preparation. The structure of Fe_3O_4 aggregates released from the NaCl matrix was

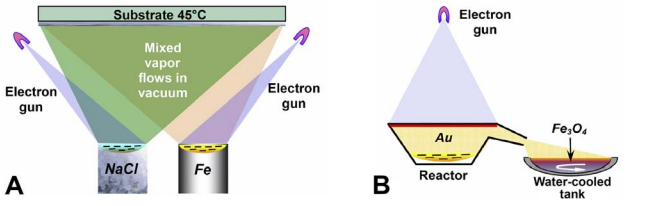

Fig. 1 Schematic representation of Fe_3O_4–Au MNC synthesis *via* EB-PVD: (A) iron and sodium chloride are vaporized by an electron beam, then the vapors condense on a cooled substrate, forming iron nanoparticles embedded in NaCl matrix; (B) following oxidation the nanoparticles are coated with gold evaporated from a reactor.

followed by transmission electron microscopy (TEM) with a HITACHI H-800 microscope (Hitachi, Japan) at 150 kV acceleration voltage. Inductively coupled plasma atomic emission spectroscopy (ICP-AES) was used to determine the concentration of gold in MNC with an Optima 2100 DV instrument (PerkinElmer, USA). Scanning electron microscope (SEM) images were taken to study the morphology and size of MNC using MIRA3 (TESCAN, Czech Republic) microscope with a field emission cathode (high-brightness Schottky cathode), energy dispersive X-ray spectrometer (EDX), X-max 80 mm^2 detector (Oxford instruments, UK), operating at an accelerating voltage of 5–20 kV. In order to investigate the crystalline structure of MNC powder, X-ray diffraction (XRD) analysis was performed using a DRON-UM1 (Burevestnik, USSR) diffractometer with a Co K_α radiation configured for focused beam Bragg–Brentano, a step scan size of 0.05° between 10–85° at 1 s exposure. Phase identification was carried out using Match! v.1.0 software (Crystal Impact, Germany) coupled with the International Centre for Diffraction Data (PDF-2).

TEM images of DOX-MNC were taken with 200 kV JEOL (Japan) JEM-ARM200F NEOARM Holographic Electron Microscopy equipped with a 4 K resolution Gatan CCD camera at the University of Salento (Lecce, Italy) and then processed with DigitalMicrograph v. 3.53.4137.0 software (Gatan Inc, USA). Histogram and heterogeneity analysis of acquired images was performed based on Moran's I spatial autocorrelation index[22] using ImageJ 1.53a (National Institutes of Health, USA) and Autocorrelation v.1.0 (NCI) software. This research was conducted within the scope of proposal 20232024 "Holo-TEM of magnetic nanocomplexes Au–Fe_3O_4-DOXO for a more effective fight against cancer", which was financed by the Central European Research Infrastructure Consortium (CERIC-ERIC).

The magnetic properties of MNC samples were determined using a 7404 vibrating-sample magnetometer (VSM) with a sensitivity of 10^{-7} emu in magnetic fields of up to 5000 Oe (Lake Shore Cryotronics Inc., USA). Weight measurements of the samples were performed with an AB135-S/FACT electronic microbalance scale with a sensitivity of 10^{-5} g (Metller Toledo, Switzerland).

MNC hydrodynamic size was assessed using a Malvern Zetasizer Nano S analyzer (Malvern Panalytical, UK) in an aqueous colloidal system. The spectrometer could measure particles ranging from 0.3 nm–10 μm with an accuracy of ±2% and sensitivity of 0.1 mg ml^{-1} (lysozyme).

2.3 DOX loading

Loading of Fe_3O_4–Au MNC with DOX (Pfizer, Italy) was carried out through the magneto-mechanochemical synthesis using a magneto-mechanical milling chamber (NCI, Ukraine) as described in ref. 23. Previously observed a 10-fold decrease in DOX size after synthesis measured at 15 kV accelerating voltage[24] was not visualized in this study at 200 kV.

2.4 Experimental animals, tumor implantation and treatment

Female noninbred rats with body weights of 123.4 ± 7.9 g were obtained from the vivarium of the National Cancer Institute (NCI, Ukraine). Animals were randomly divided into four experimental groups ($n = 5$): (1) control group undergoing no treatment; (2) group treated with conventional DOX; (3) group given DOX-MNC; (4) group receiving DOX-MNC and exposed to CMF and EMF. All rats were implanted with Walker-256 carcinosarcoma cells (2×10^6 in medium 199) by intramuscular injection into the right hindlimb. Walker-256 carcinosarcoma is a rapidly growing experimental model with patterns of both carcinoma and sarcoma, extensively studied and validated to reliably induce tumor growth in experimental animals.[25,26] The current work was designed according to the research recommendations outlined in ref. 27.

In groups 2–4, 1.5 mg kg^{-1} DOX or 3 mg kg^{-1} Fe_3O_4–Au MNC loaded with 1.5 mg kg^{-1} DOX was administered by intravenous injection every other day (five times in total) starting on day 2 after tumor implantation. Prior to CMF and EMF treatment, rats in group 4 were anesthetized with 1–2% isoflurane inhalation and immobilized. Tumor-bearing animals were exposed to 42 MHz EMF generated using an experimental prototype of a MagTherm medical device (Radmir, Ukraine) for 15 min following intravenous administration of DOX-MNC. We placed a previously designed magnetic dipole applicator, comprising an array of needle-shaped dipole antennas and NdFeB permanent magnet with a field strength of 30 mT,[28] under the tumor during EMF treatment in order to produce a nonuniform CMF and thus target DOX-MNC to the tumor site by the field gradient. Recordings of tumor temperature, as measured by TM-4 fiber optical thermometer (Radmir, Ukraine), did not exceed 39 °C in response to 15 min electromagnetic irradiation, which maintained more physiological conditions of moderate hyperthermia.[23]

This study was approved by the NCI Regional Committee for Animals and Medical Research Ethics. All animal procedures were carried out in accordance with the Law of Ukraine N 3447-IV and European Directive 2010/63/EU.

2.5 Nonlinear growth kinetics of Walker-256 carcinosarcoma

Once palpable, tumors were measured in three orthogonal dimensions: length, width and height using a digital caliper.[29] Tumor volumes were estimated assuming an ellipsoid shape according to the following equation:

$$V = L \times W \times H \times \pi/6$$

where L is the length, W is the width and H is the height of the tumor.

Differences in nonlinear tumor growth kinetics between experimental groups were measured with respect to the role of free radicals using the growth factor φ and breaking ratio κ.[30]

2.6 Magnetic resonance imaging

MRI studies were carried out at a magnetic field strength of 1.5 T and transmission frequency of 63.9 MHz (Intera, Philips, the Netherlands) using an 8-channel knee coil array (Sense Knee Coil, Philips). Animals were anesthetized with isoflurane

inhalation prior to image acquisition. ^{1}H MRI scans were weighted according to the T_1 (spin–lattice) relaxation time (repetition time (TR)/echo time (TE) = 500/18 ms, slice thickness = 2.5 mm) and T_2 (spin–spin) relaxation time (TR/TE = 3230/100 ms, slice thickness = 2.5 mm). Imaging findings of tumor necrosis, intratumoral hemorrhage and peritumoral edema were compared between animal groups based on ref. 31 and 32.

Since Fe_3O_4–Au nanoparticles are generally suitable to serve as T_2 contrast agents,[33] circular regions of interest (ROIs) were drawn on the acquired T_2-weighted (T_2W) coronal images: tumor (1), muscle (2) and background (3) with Horos 4.0 software (Horos Project, Switzerland). The center of the tumor ROI was defined as the intersection of the two longest diameters; the center of the muscle ROI matched the intersection point of the two longest diameters of the hamstring muscle in the contralateral limb. In choosing the background ROI, we avoided regions that might contain motion artifacts.[34] Given ROI intensity measurements, image contrast in the tumor was calculated as follows:

$$\text{Image contrast} = (\text{ROI}_{\text{tumor}} - \text{ROI}_{\text{background}})/\text{ROI}_{\text{background}}.$$

2.7 Electron spin resonance spectroscopy

ESR spectra of tissue specimens were recorded on a RE1307 spectrometer using a cylindrical resonator with H011 mode at 9.09 GHz. Instrument settings: temperature 77 K, microwave power 40 mW, modulation frequency 100 kHz. Tumor and muscle tissue specimens were placed in a quartz Dewar with an inner diameter of 4.5 mm. ESR signals were distinguished on the basis of *g*-factors, as described in ref. 35. Levels of free radicals, including ubisemiquinone, superoxide ($O_2^{\bullet -}$) and nitric oxide ($^{\bullet}$NO), were interpreted according to ref. 36–38.

2.8 Statistical analysis

The Kolmogorov–Smirnov test was used to assess the normality of data distributions. Mann–Whitney *U* test was used to compare TEM image brightness and Moran's spatial autocorrelation. One-way analysis of variance (ANOVA) followed by Tukey HSD multiple comparisons were performed to analyze the tumor growth factor and ESR signals. ROI intensities on MRI scans were compared between groups by the Kruskal–Wallis test. Significance was determined at the $p < 0.05$ level. All statistical analyses were conducted using SPSS Statistics v. 25.0 (IBM, Inc., Armonk, NY, 2017).

3. Results and discussion

3.1 Microstructure and composition of Fe_3O_4–Au MNC

Fig. 2 shows a TEM image of Fe_3O_4 nanoparticles prior to gold coating. In Fig. 2A the nanoparticles are spherical and have a narrow size distribution, while their microdiffraction pattern (Fig. 2B) demonstrates a high degree of crystallinity and uniformity. XRD indicated that the crystallite size of the Fe_3O_4 phase was 13 nm. Fig. 3 shows SEM images of magnetite nanoparticles after gold coating, with increasing magnification from (A) to (B). The produced sample of MNC powder displayed a structure comprised of Au nanoparticles with an average diameter of 13 nm deposited in a discontinuous manner on the surface of Fe_3O_4 aggregates (≤200 nm). The presence of gold (944 ppm) in MNC was confirmed by ICP-AES. It should be noted that Fe_3O_4 nanoparticles bore island structures of Au on their surface rather than a continuous shell, which would otherwise completely reduce the reactivity of MNC and prevent the formation of DOX-induced ROS in the tumor and its microenvironment[39] under the influence of CMF + EMF. A contributing factor here could also be the charge transfer from Au to Fe_3O_4 surface atoms. Alterations in Fe^{2+} and Fe^{3+} ordering lead to oxygen release as a result of magnetite reduction at the interface with gold.[40] Moreover, continuous and thick gold shells were found to reduce the contrasting capability of Fe_3O_4–Au MNC for MRI.[41]

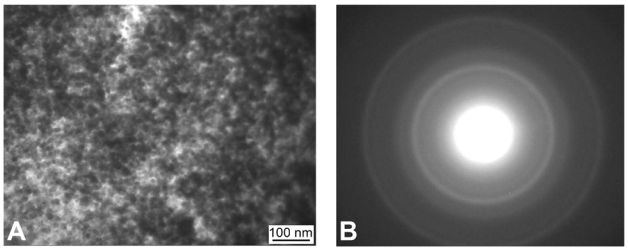

Fig. 2 TEM image (A) and electron pattern (B) of Fe_3O_4 nanoparticles synthesized using EB-PVD.

To investigate changes in MNC structure after DOX loading, TEM images were taken with a JEM-ARM200F NEOARM Holographic Electron Microscope. Fig. 4 shows the formation of monocrystalline MNC given visible interplanar distances on individual nanoparticles (Fig. 4A, A′, B and B′) and corresponding fast-Fourier-transform (FFT) images (Fig. 4C and D). Quantitative analysis of the acquired image series revealed that DOX loading by magneto-mechanochemical synthesis increased the average image brightness from 89 ± 0.2 a.u. to 120 ± 0.2 a.u., decreased Moran's spatial autocorrelation index from 0.58 ± 0.01 a.u. to 0.45 ± 0.01 a.u. ($p < 0.05$) and slightly affected the size

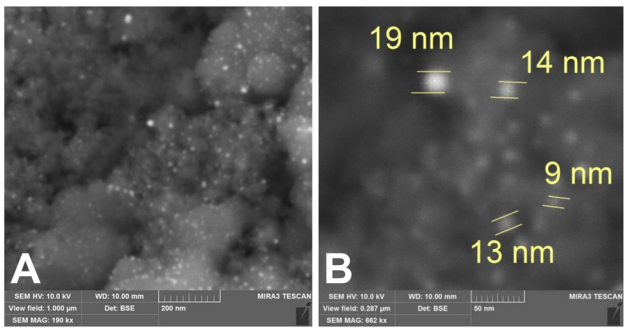

Fig. 3 SEM images with increasing magnification from (A) and (B) of Fe_3O_4–Au MNC: EB-PVD formed island structures of gold (bright spots) on the surface of magnetite nanoparticles (dark spots).

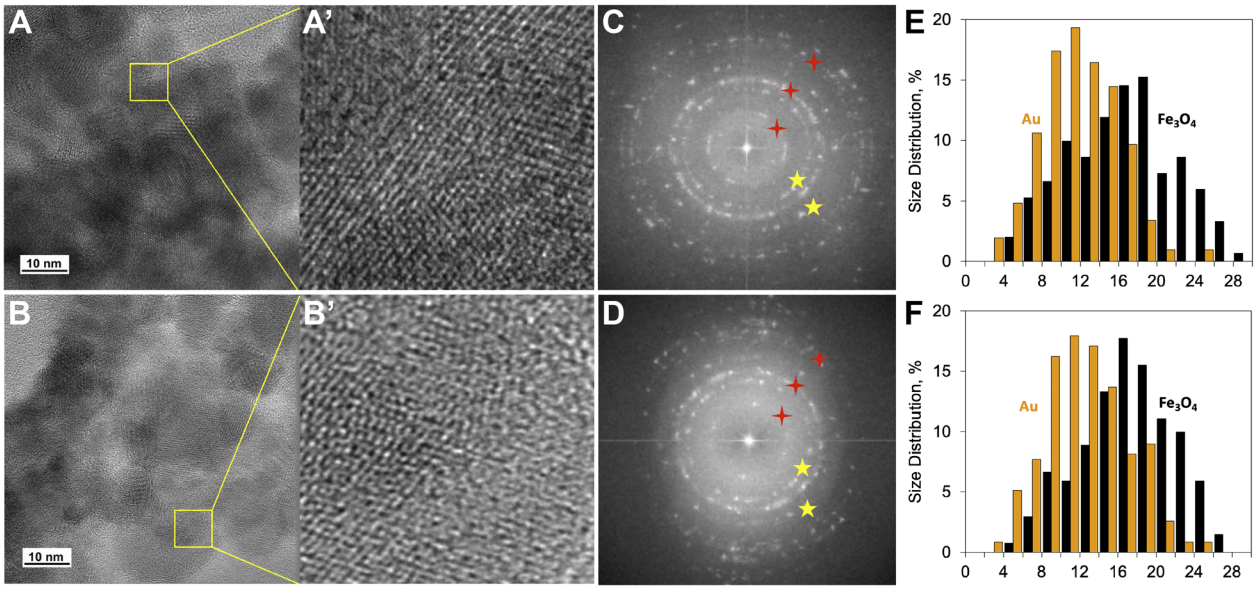

Fig. 4 TEM, FFT images and size distributions of Fe_3O_4–Au MNC before (A, A′, C and E) and after DOX loading (B, B′, D and F): TEM images with increasing magnification from A to A′ and B to B′; FFT images (C and D): yellow marks correspond to the contributions of gold and red marks correspond to the contributions of Fe_3O_4; size (nm) distributions (E and F) of Au and Fe_3O_4 nanoparticles comprising MNC.

distribution of MNC (Fig. 4E and F). Au nanoparticles had an average size of 11 nm, whereas Fe_3O_4 nanoparticles had an average size of 17 nm. A 1.4-fold increase in the average brightness of TEM images following DOX loading reflects a change in the distribution density of incident electrons, and given the coupling between electric and magnetic properties a change in reactivity of the resulting MNC can be expected.[42] A 22% lower value of Moran's index after DOX loading indicates a greater degree of MNC heterogeneity. There are several sources of DOX-MNC heterogeneity that have an impact on its reactivity: stochastic, interparticle and intraparticle. The former refers to the nonlinear nature of DOX distribution on the MNC surface; the latter are associated with heterogeneity of spatial organization between Au and Fe_3O_4 nanoparticles as well as variation in size and surface chemistry of MNC.[43]

The hydrodynamic size of the synthesized Fe_3O_4–Au MNC transferred into an aqueous solution is shown in Fig. 5. The mechanism by which gold nanoparticles aggregate is quite different from magnetite nanoparticles, where the attraction between the particles is not only due to ionic species in the solution but also their magnetic moments. In line with ref. 44, DOX-MNC was stable for 30 days under normal storage conditions. It was also shown that aggregation of Fe_3O_4 nanoparticles coated with Au varied depending on the concentration of gold added during synthesis.[45]

3.2 Magnetic properties of Fe_3O_4–Au MNC

The magnetic hysteresis loop for Fe_3O_4–Au MNC measured at room temperature is presented in Fig. 6. MNC shows behavior like a ferromagnetic material with the saturation magnetic moment (m_s) of 50.9 emu g^{-1} and coercivity (H_c) at 63 Oe. While it is possible that the electron transfer processes at the Fe_3O_4/Au interface induce local changes in magnetization, the observed

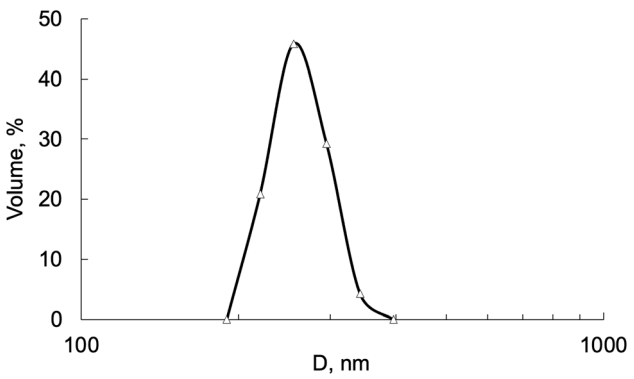

Fig. 5 Hydrodynamic size (D) of Fe_3O_4–Au MNC in aqueous solution.

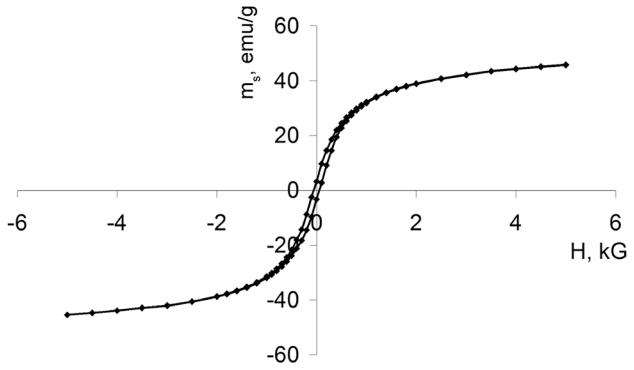

Fig. 6 Magnetic hysteresis loop measured for Fe_3O_4–Au MNC at room temperature.

Table 1 Physicochemical properties of Fe_3O_4–Au MNC synthesized by EB-PVD[a]

d_{cr}, nm	13
Fe, wt%	96.7
Au content, ppm	944
M_s, emu g^{-1}	50.9
M_{sFe}, emu g^{-1}	52.7
M_r, emu g^{-1}	3.69
M_{rFe}, emu g^{-1}	3.81
H_c, Oe	63
D, nm	263

[a] d_{cr} – average crystallite size, M_s – saturation magnetization, M_{sFe} – saturation magnetization calculated for iron, M_r – remnant magnetization, M_{rFe} – remnant magnetization calculated for iron, H_c – coercive force, D – hydrodynamic size in aqueous solution.

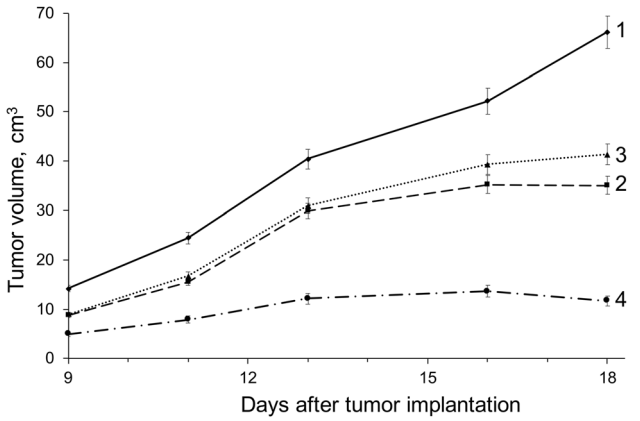

Fig. 7 Growth kinetics of Walker-256 carcinosarcoma: (1) – control (no treatment); (2) – DOX; (3) – DOX-MNC; (4) – DOX-MNC + CMF + EMF.

magnetic properties are mainly attributed to iron oxide.[46] Our previous study found that DOX alone was a diamagnetic substance that did not significantly change the magnetic properties of DOX-MNC after loading.[23]

The magnetic properties of Fe_3O_4 nanoparticles are determined by a number of factors such as crystalline size, shape and domain structure. Bulk ferromagnets consist of many domains in order to minimize their total magnetic energy under the influence of an external CMF. The boundaries between adjacent domains are formed by domain walls in which the direction of magnetization changes between different minima of the crystalline anisotropy.[47] As the particle size decreases, energy considerations no longer favor their division into domains and thus a transition from a multidomain to a single domain state may occur. Importantly, spherical Fe_3O_4 nanoparticles tend to be single domain at the critical size of 128 nm.[48,49] We report that the average size of Fe_3O_4 crystallites did not exceed 13 nm in the synthesized MNC. Single domain nanoparticles are uniformly magnetized due to a coherent rotation of the majority of their magnetic moments displaying high coercivity and remanent magnetization. The measured coercivity is linked with the effective anisotropy constant as follows:

$$H_c = 2K/M_s$$

where K is the effective anisotropy constant, M_s is the saturation magnetization.

Smaller nanoparticles have a larger surface to volume ratio that confers their reactivity and gives rise to magnetic anisotropy contributions from the surface layer.[50] Furthermore, aggregation of MNC with a discontinuous coating, as shown in Fig. 3 and 4, is also associated with changes in the effective anisotropy.[51] Although the size of Fe_3O_4 crystallites may have suggested the superparamagnetic properties of MNC, it appeared that the magnetic anisotropy energy barrier was not overcome by the thermal activation energy or the applied magnetic field. Taken together, the investigated MNC exhibited ferromagnetic behavior. Table 1 summarizes the physicochemical properties of synthesized Fe_3O_4–Au MNC with discontinuous gold shell for prevention of aggregation, better MRI contrasting and initiation of ROS.

3.3 Walker-256 carcinosarcoma growth kinetics and host body weight

Walker-256 carcinosarcoma growth kinetics are shown in Fig. 7 and Table 2. Growth rates were determined over 18 days following implantation because this tumor model undergoes all three stages of development (initiation, promotion and progression) within a short period of time.[52] Our observations indicate that treatment with DOX-MNC under the influence of CMF + EMF had the most pronounced inhibitory effect on Walker-256 carcinosarcoma growth kinetics. Evidence of this includes 14% and 16% higher values of the breaking ratio in response to DOX-MNC + CMF + EMF compared with DOX action alone and DOX-MNC, respectively. However, there was no significant difference in the growth factor values between

Table 2 Treatment effect on Walker-256 carcinosarcoma growth kinetics 18 days after implantation, $M \pm m$

Group	Treatment	Growth factor φ, per day	Breaking ratio κ, r.u.
1	Control (no treatment)	0.66 ± 0.009	1.00
2	DOX	0.58 ± 0.003^{a}	1.13
3	DOX-MNC	0.60 ± 0.003^{a}	1.11
4	DOX-MNC + CMF + EMF	$0.50 \pm 0.003^{a,b,c}$	1.32

[a] Significant difference from control, $p < 0.05$. [b] Significant difference from DOX, $p < 0.05$. [c] Significant difference from DOX-MNC, $p < 0.05$.

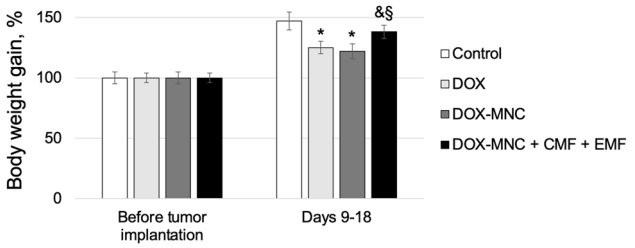

Fig. 8 Changes in body weight of Walker-256 carcinosarcoma-bearing animals relative to their weight before implantation. *Significant difference from control, $p < 0.05$; &significant difference from DOX, $p < 0.05$; §significant difference from DOX-MNC, $p < 0.05$.

groups receiving DOX-MNC and DOX, which were 12% and 9% lower than in the untreated control group ($p < 0.05$). This can be explained by changes in the generation of different levels of free radical species in response to free DOX and DOX-MNC, as compared with those under CMF and EMF.

Tumor growth kinetics has been previously shown to influence the prognosis for cancer patients: tumors with larger growth factor values are typically more resistant to chemotherapy and have increased recurrence rates.[53] The results from this study provide further confirmation of earlier *in vitro* experiments in which Fe_3O_4–Au nanostructures loaded with DOX were found to exert antitumor effects *via* nonthermal and thermal mechanisms underlying the action of CMF and EMF.[54–56]

Changes in body weight of Walker-256 carcinosarcoma-bearing rats relative to their weight prior to tumor implantation are shown in Fig. 8. There was no significant difference in the host body weight between animal groups before the implantation. The control group receiving no treatment showed the highest gain in total body weight during the study period. DOX and DOX-MNC resulted in nearly 25% lower weight gain than animals in the control group ($p < 0.05$), in agreement with previous work in which Walker-256 carcinosarcoma-bearing animals demonstrated less weight gain in response to chemotherapeutic agents than those receiving no treatment.[57,58] DOX-MNC + CMF + EMF did not significantly affect the host body weight when compared with the control group.

3.4 Magnetic resonance imaging

Representative T_2W whole-body MRI scans obtained from Walker-256 carcinosarcoma-bearing rats are shown in Fig. 9.

MRI visualization revealed the least pronounced necrotic changes and the greatest extent of peritumoral edema in control tumors as compared with any of the treated groups. DOX-MNC + CMF + EMF led to more extensive regions of central tumor necrosis than DOX alone or DOX-MNC. In addition, MRI findings of intratumoral hemorrhage were observed to a greater degree in the control and DOX-MNC + CMF + EMF groups. This can be explained by elevated interstitial fluid pressure and mechanical compression during tumor growth in animals receiving no treatment or the magnetic force produced by DOX-MNC under the influence of CMF and EMF.[59,60]

Fig. 10 shows the results of histogram analysis for tumor ROIs delineated on T_2W MRI scans. Pixel distribution in ROIs from all experimental groups was not normal ($p < 0.05$).

Histogram features, skewness and kurtosis, extracted from the control tumors demonstrated the largest values, which are associated with increased tumor heterogeneity and poorer prognosis in cancer patients.[61] DOX-MNC or DOX-MNC + CMF + EMF had a flatter distribution than the control or DOX group. Not only did DOX-MNC + CMF + EMF action result in negative skewness of tumor ROIs but also the lowest absolute value among other groups. In the latter situation, we cannot neglect the possibility that DOX-MNC distribution could match the chaotic structure of the tumor and the microenvironment in the

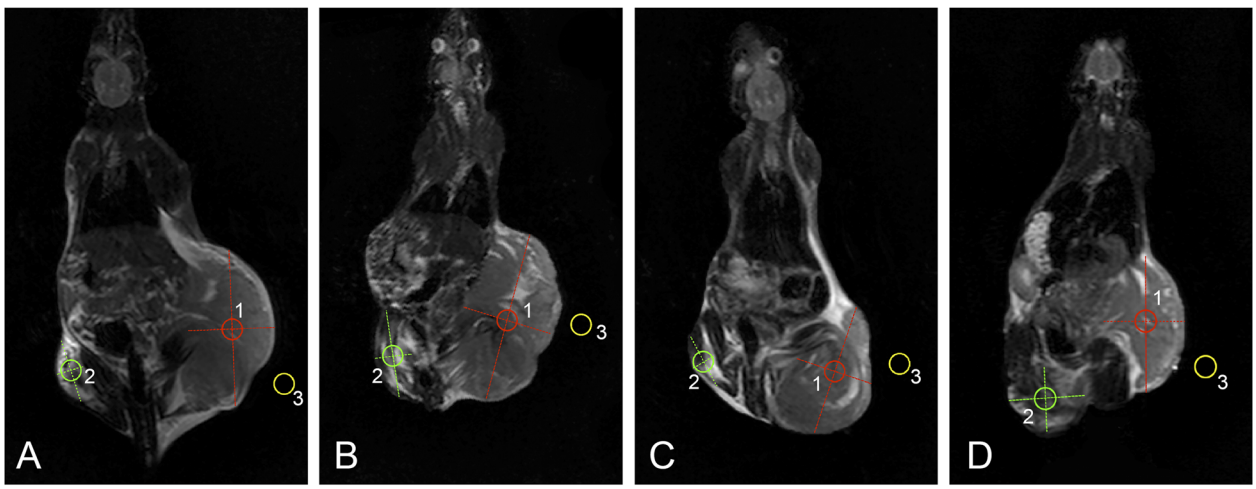

Fig. 9 Representative T_2W coronal whole-body MRI scans of Walker-256 carcinosarcoma-bearing rats acquired at 18 days after tumor implantation: control (A), DOX (B), DOX-MNC (C), DOX-MNC + CMF + EMF (D). Red circles (1) indicate the tumor ROI; green circles (2) denote the muscle ROI in the contralateral limb; yellow circles outline the background ROI (3).

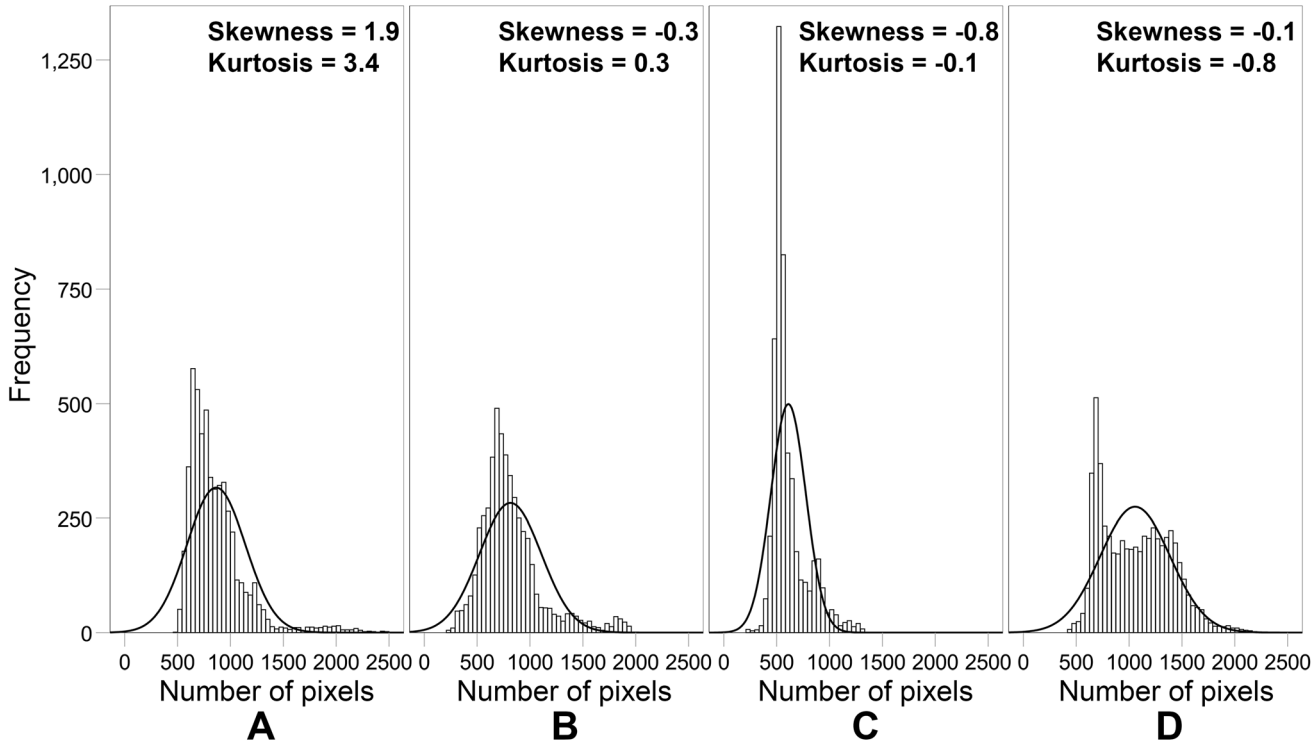

Fig. 10 Image histograms of tumor ROIs on T_2W MRI scans: control (A); DOX (B); DOX-MNC (C); DOX-MNC + CMF + EMF (D).

Table 3 Comparison of ROI intensity on T_2W MRI scans obtained from Walker-256 carcinosarcoma-bearing rats, median (min; max)

Group	Tumor, a.u.	Muscle, a.u.	Background, a.u.	Tumor/muscle ratio	Tumor contrast
Control	794.6 (519.4; 2476.7)	1268.4 (130.7; 3997.1)	36.1 (0; 141.0)	0.6	21.0
DOX	693.4^{a} (285.6; 1358.0)	706.0^{a} (150.9; 2518.5)	41.3^{a} (0; 111.4)	1.0	15.8
DOX-MNC	$609.1^{a,b}$ (217.3; 1333.9)	$317.0^{a,b}$ (37.4; 2368.7)	$26.7^{a,b}$ (0; 119.3)	1.9	21.8
DOX-MNC + CMF + EMF	$1110.3^{a,b,c}$ (429.0; 1769.5)	$805.6^{a,b,c}$ (154.7; 3945.8)	$42.4^{a,b,c}$ (0; 112.3)	1.4	25.2

[a] Significant difference from control, $p < 0.05$. [b] Significant difference from DOX, $p < 0.05$. [c] Significant difference from DOX-MNC, $p < 0.05$.

presence of a nonuniform CMF, leading to the observed difference in skewness on MRI.

Quantitative analysis of ROI intensity on T_2W images is summarized in Table 3. Intravenous administration of DOX and DOX-MNC led to a significantly lower intensity of both the tumor and the muscle tissue in the contralateral limb. On the contrary, there was a substantial increase in the image intensity of tumor ROIs following DOX-MNC + CMF + EMF as compared with the control (1.4 times), conventional DOX (1.6 times) and DOX-MNC (1.8 times) groups. The ratio of the tumor ROI intensity to the intensity of the muscle ROI changed across the groups from 0.6 (control) to 1.9 (DOX-MNC). We also note that the image contrast of DOX-MNC + CMF + EMF tumors was 1.2 times as much as in the control group. In the previous work, Fe_3O_4–Au nanostructures were observed to produce a local inhomogeneity of the applied field and thereby shortening T_2 relaxation time, once delivered to the tumor.[62]

3.5 Electron spin resonance spectroscopy

A comparison of ESR spectra and free radical levels recorded from Walker-256 carcinosarcoma are shown in Fig. 11 and 12. Signals measured in the tumor samples occurred around $g = 2.007$, indicating that free electron spins were present in the triplet state. Further analysis of ESR spectra revealed that the highest levels of free radicals were measured in the control group. As a result of DOX-MNC + CMF + EMF treatment, there was only a 7% difference in the nitric oxide level between the tumor and the muscle tissue in the contralateral limb ($p < 0.05$). Overall, DOX, DOX-MNC and DOX-MNC + CMF + EMF led to a 47% reduction, on average, in the level of ubisemiquinone, superoxide radical and nitric oxide in the tumor compared with the control group. Interestingly, the differences in superoxide and nitric oxide levels between the groups were in agreement with the direction of changes in the extent of peritumoral edema on MRI. It has been reported in previous studies that

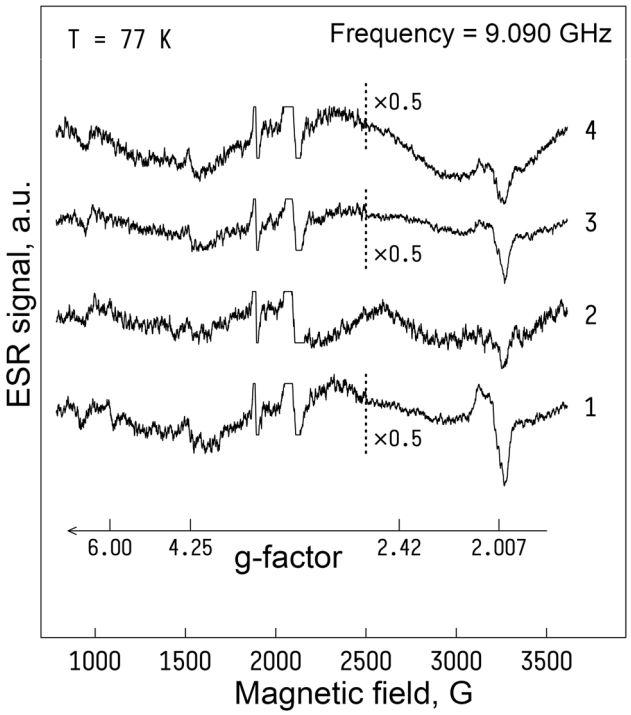

Fig. 11 Electron spin resonance spectra of Walker-256 carcinosarcoma 18 days after implantation: (1) – control (no treatment); (2) – DOX; (3) – DOX-MNC; (4) – DOX-MNC + CMF + EMF; $T = 77$ K.

superoxide and nitric oxide are implicated in neoangiogenesis, vasodilation and peritumoral edema formation.[63,64]

A high level of free radicals is thought to have detrimental consequences on cell function and survival, whereas at moderate and low levels they mediate redox signaling pathways. In particular, overwhelming superoxide and nitric oxide production has been found to rapidly lead to necrotic cell death, as opposed to the initiation of apoptotic cell signaling under mild oxidative stress.[65–67] At physiological levels, superoxide radical and nitric oxide are also involved in signaling pathways that regulate muscle tissue remodeling, repair and regeneration.[68,69] As is the case with many processes in biological systems, it is important to take into account the nonlinearity of free radical initiation in mitochondria and their role in cellular responses.[70] These aspects of ROS and RNS function explain why DOX-MNC + CMF + EMF demonstrated a notable decrease in ubisemiquinone, superoxide and nitric oxide levels in Walker-256 carcinosarcoma.

Since free radicals contain unpaired electrons in the outer shell, they tend to be extremely reactive, enabling interactions with most cellular macromolecules, such as proteins, DNA and lipids. Many of the well-established strategies for cancer treatment aim to modulate free radical levels in the tumor and its microenvironment. For instance, the accumulation of DOX in tumor cells leads to ROS elevation. DOX can be reduced to its semiquinone radical by the cytochrome P450 system and the electron transport chain in mitochondria. Semiquinone radicals have a half-life of several days at 37 °C retained as relatively stable radicals. However, semiquinone still serves as an electron donor in the vicinity of molecular oxygen giving rise to superoxide formation that itself is subject to redox cycling with hydrogen peroxide (H_2O_2) and hydroxyl radical ($^{\bullet}OH$) formation.[71,72] Superoxide is involved in the regulation of nitrogen oxide and peroxynitrite ($ONOO^-$) levels; the latter is a powerful and toxic oxidant.[73] In addition, DOX contributes to mitochondrial iron overload by redox cycling between Fe^{2+} and Fe^{3+} ions which in turn induces the generation of hydroxyl radicals *via* the Fenton and Haber–Weiss reactions. Oxidative stress thus represents one of the mechanisms proposed for toxicity associated with MNC composed of iron oxide.[39] It should also be noted that electromagnetic irradiation alone can change the kinetics and yields of free radical reactions, leading to some level of tumor growth inhibition.[74,75]

Based on our earlier works,[23,28,76] we applied a nonuniform CMF and radiofrequency EMF in order to target DOX-MNC distribution and influence free radical reactions in the tumor through changes in spin-regulated electron and proton transport in mitochondria. Comparative analysis of ESR and MRI results indicates a possible relationship between electron and proton transfer processes in biochemical reactions underlying Walker-256 carcinosarcoma response to DOX-MNC + CMF + EMF treatment. The unpaired electrons could interact with protons under electromagnetic irradiation during ESR and ^1H MRI. Therefore, the observed changes in ESR spectra and intensity of tumor ROIs in MRI scans may be linked by the hyperfine interaction between the magnetic moment of the electron in a free radical produced by DOX-MNC and nuclear spins.[77] This is further supported by the ability of DOX and ROS to alter T_2 relaxation time and image intensity on MRI.[78,79]

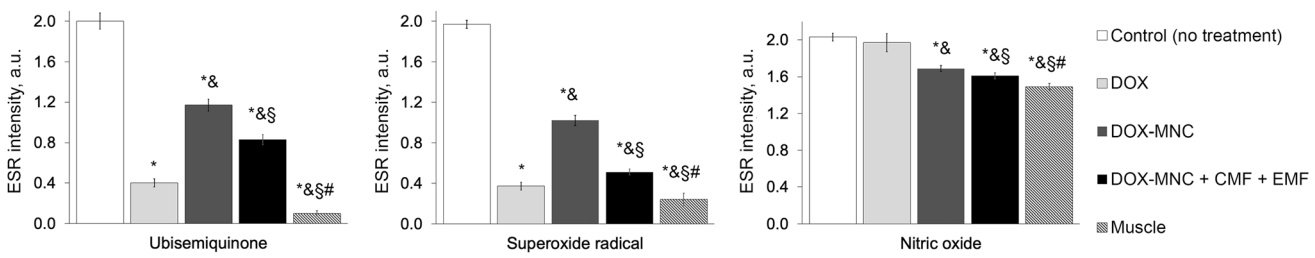

Fig. 12 Redox state in Walker-256 carcinosarcoma 18 days after implantation: *significant difference from control, $p < 0.05$; $^{\&}$significant difference from DOX, $p < 0.05$; §significant difference from DOX-MNC, $p < 0.05$; $^{\#}$significant difference from DOX-MNC + CMF + EMF, $p < 0.05$.

4. Conclusions

In summary, our results demonstrate that DOX-MNC can be prepared using EB-PVD in combination with magneto-mechanochemical synthesis for cancer nanotheranostic applications. Characterization of MNC involved several methods, including TEM, SEM, ICP-AES, XRD analysis, VSM and spectrophotometry. We found that a discontinuous gold coating deposited on spherical magnetite nanoparticles had negligible effects on the ferromagnetic properties of the resulting Fe_3O_4–Au MNC. Following DOX loading, we investigated the antitumor effect of DOX-MNC on Walker-256 carcinosarcoma under the influence of a nonuniform CMF and radiofrequency EMF by comparing tumor growth kinetics, MRI scans and ESR spectra. DOX-MNC + CMF + EMF treatment caused a 14% and 16% more pronounced inhibitory effect on Walker-256 carcinosarcoma growth kinetics than DOX and DOX-MNC alone, respectively. MRI visualization revealed more substantial tumor necrotic changes in response to DOX-MNC combined with CMF and EMF than in the control, DOX or DOX-MNC groups. Furthermore, quantitative analysis of T_2W MRI scans showed a significant increase in image intensity of tumor ROIs in the DOX-MNC + CMF + EMF group as compared with the control (1.4 times), conventional DOX (1.6 times) and DOX-MNC (1.8 times) groups. Pixel distribution of tumor ROIs had the lowest absolute value of skewness after DOX-MNC + CMF + EMF. Although the level of ubisemiquinone radical, superoxide radical and nitric oxide measured by ESR spectroscopy in the tumor was on average 47% lower in response to any of the given treatments than in the control group, DOX-MNC + CMF + EMF resulted in the lowest level of nitric oxide, which was close to that of the muscle tissue in the contralateral limb. The observed differences in superoxide and nitric oxide levels between experimental groups matched with the direction of changes in the extent of peritumoral edema on MRI. In principle, the relationship between changes in ESR spectra and intensities of MRI scans may be explained by the hyperfine interaction between the magnetic moment of the electron in a free radical generated by DOX-MNC in mitochondria and nuclear spins. Future studies should therefore support the translation of DOX-MNC prepared using EB-PVD in combination with magneto-mechanochemical synthesis from preclinical to clinical development as an MRI contrast agent and a remotely controlled drug delivery platform under CMF and EMF by giving rise to a clearer understanding of the spin-regulated electron and proton transport in DOX-MNC, tumor and its microenvironment.

Author contributions

Valerii B. Orel: conceptualization; data curation; formal analysis; investigation; methodology; software; visualization; writing – original draft; writing – review & editing. Yurii A. Kurapov: conceptualization; methodology; supervision; project administration; validation. Stanislav Ye. Lytvyn: investigation; methodology; formal analysis; visualization; writing – review & editing. Valerii E. Orel: conceptualization; methodology; supervision; project administration; validation; writing – review & editing. Olexander Yu. Galkin: validation; project administration. Olga Yo. Dasyukevich: investigation. Oleksandr Yu. Rykhalskyi: investigation. Anatoliy G. Diedkov: resources; funding acquisition; project administration. Vasyl V. Ostafiichuk: resources; funding acquisition; project administration. Sergii A. Lyalkin: resources; funding acquisition; project administration. Anatoliy P. Burlaka: investigation. Sergii V. Virko: investigation. Mykola A. Skoryk: investigation. Viacheslav V. Zagorodnii: Investigation. Yaroslav A. Stelmakh: resources. Gennadii G. Didikin: formal analysis; resources. Olena I. Oranska: formal analysis. Lucio Calcagnile: data curation; visualization. Daniela E. Manno: investigation; visualization; writing – review & editing. Rosaria Rinaldi: investigation; visualization. Yana V. Nedostup: formal analysis.

Conflicts of interest

Authors declare no conflicts of interest.

Acknowledgements

This research was partially funded by the Ministry of Health of Ukraine: To develop a method of antitumor therapy of primary malignant bone tumors based on magnetochemical technology using nanocomplexes (code BH.14.01.07.204-23, registration number 0123U100711) and Improvement of conservative treatment results for breast cancer patients with low or negative HER2/neu status based on optimization and personalization of therapy methods (code BH.14.01.07.205-23, registration number 0123U100713). The authors acknowledge the CERIC-ERIC Consortium for the access to Transmission Electron Microscope 200 kV JEOL (Japan) JEM-ARM200F NEOARM Holographic Electron Microscopy at the University of Salento (Lecce, Italy) and financial support of proposal 20232024 "Holo-TEM of magnetic nanocomplexes Au–Fe_3O_4-DOXO for a more effective fight against cancer".

References

1 O. L. Gobbo, K. Sjaastad, M. W. Radomski, Y. Volkov and A. Prina-Mello, Magnetic nanoparticles in cancer theranostics, *Theranostics*, 2015, **5**, 1249–1263, DOI: **10.7150/thno.11544**.

2 S. V. Gorobets, O. Yu. Gorobets and S. O. Kovalova, Bioinformatic analysis of the genetic mechanism of biomineralization of biogenic magnetic nanoparticles in bacteria capable of tumor-specific accumulation, *Innovative Biosyst. Bioeng.*, 2022, **6**, 48–55, DOI: **10.20535/ibb.2022.6.2.260183**.

3 S. M. Dadfar, K. Roemhild, N. I. Drude, S. Von Stillfried, R. Knüchel, F. Kiessling and T. Lammers, Iron oxide nanoparticles: Diagnostic, therapeutic and theranostic applications, *Adv. Drug Delivery Rev.*, 2019, **138**, 302–325, DOI: **10.1016/j.addr.2019.01.005**.

4 F. Soetaert, P. Korangath, D. Serantes, S. Fiering and R. Ivkov, Cancer therapy with iron oxide nanoparticles: Agents of thermal and immune therapies, *Adv. Drug Delivery Rev.*, 2020, **163–164**, 65–83, DOI: **10.1016/j.addr.2020.06.025**.

5 W. W. Gan, L. W. Chan, W. Li and T. W. Wong, Critical clinical gaps in cancer precision nanomedicine

development, *J. Controlled Release*, 2022, **345**, 811–818, DOI: **10.1016/j.jconrel.2022.03.055**.

6 H. Zeng and S. Sun, Syntheses, properties, and potential applications of multicomponent magnetic nanoparticles, *Adv. Funct. Mater.*, 2008, **18**, 391–400, DOI: **10.1002/adfm.200701211**.

7 T. Labouret, J. F. Audibert, R. B. Pansu and B. Palpant, Plasmon-assisted production of reactive oxygen species by single gold nanorods, *Small*, 2015, **11**, 4475–4479, DOI: **10.1002/smll.201500509**.

8 V. B. Orel, O. Yu. Galkin, V. E. Orel, O. Yo. Dasyukevich, O. Yu. Rykhalskyi, Yu. A. Kurapov, S. A. Litvin, V. O. Yukhymchuk, O. F. Isayeva, L. A. Syvak and A. G. Dedkov, Mechanoluminescence of Walker-256 carcinosarcoma cells induced by magneto-mechanochemical effects of Fe_3O_4-Au nanocomposite, *J. Mech. Med. Biol.*, 2023, **2340027**, 1–16, DOI: **10.1142/S0219519423400274**.

9 P. Saura and V. R. I. Kaila, Energetics and dynamics of proton-coupled electron transfer in the NADH/FMN site of respiratory complex I, *J. Am. Chem. Soc.*, 2019, **141**, 5710–5719, DOI: **10.1021/jacs.8b11059**.

10 O. Cauli, Oxidative stress and cognitive alterations induced by cancer chemotherapy drugs: A scoping review, *Antioxidants*, 2021, **10**, 1116, DOI: **10.3390/antiox10071116**.

11 C. Li, T. Chen, I. Ocsoy, G. Zhu, E. Yasun, M. You, C. Wu, J. Zheng, E. Song, C. Z. Huang and W. Tan, Gold-coated Fe_3O_4 nanoroses with five unique functions for cancer cell targeting, imaging and therapy, *Adv. Funct. Mater.*, 2014, **24**, 1772–1780, DOI: **10.1002/adfm.201301659**.

12 S. Rajkumar and M. Prabaharan, Multi-functional core-shell Fe_3O_4@Au nanoparticles for cancer diagnosis and therapy, *Colloids Surf., B*, 2019, **174**, 252–259, DOI: **10.1016/j.colsurfb.2018.11.004**.

13 M. Ghorbani, F. Mahmoodzadeh, P. Nezhad-Mokhtaric and H. Hamishehkar, A novel polymeric micelle-decorated Fe_3O_4/Au core–shell nanoparticle for pH and reduction-responsive intracellular co-delivery of doxorubicin and 6-mercaptopurine, *New J. Chem.*, 2018, **42**, 18038–18049, DOI: **10.1039/C8NJ03310B**.

14 V. E. Orel, Biological mechanochemiemission and bioenergetics, *Bioelectrochem. Bioenerg.*, 1998, **46**, 273–278, DOI: **10.1016/S0302-4598(98)00133-0**.

15 V. B. Orel, A. S. Papazoglou, C. Tsagkaris, D. V. Moysidis, S. Papadakos, O. Y. Galkin, V. E. Orel and L. A. Syvak, Nanotherapy based on magneto-mechanochemical modulation of tumor redox state, *Wiley Interdiscip. Rev.: Nanomed. Nanobiotechnol.*, 2023, **15**, e1868, DOI: **10.1002/wnan.1868**.

16 Y. A. Kurapov, E. M. Vazhnichaya, S. E. Litvin, S. M. Romanenko, G. G. Didikin, T. A. Devyatkina, Y. V. Mokliak and E. I. Oranskaya, Physical synthesis of iron oxide nanoparticles and their biological activity in vivo, *SN Appl. Sci.*, 2019, **1**, 102, DOI: **10.1007/s42452-018-0110-z**.

17 M. Huth, F. Porrati and O. V. Dobrovolskiy, Focused electron beam induced deposition meets materials science, *Microelectron. Eng.*, 2018, **185–186**, 9–28, DOI: **10.1016/j.mee.2017.10.012**.

18 G. Gonzalez-Martinez, A. Bachmatiuk, V. Bezugly, J. Kunstmann, T. Gemming, Z. Liu, G. Cunibertic and M. H. Rümmeli, Electron-beam induced synthesis of nanostructures: A review, *Nanoscale*, 2016, **8**, 11340–11362, DOI: **10.1039/c6nr01941b**.

19 Y. A. Kurapov, S. Y. Lytvyn, G. G. Didikin and S. M. Romanenko, Electron-beam physical vapor deposition of iron nanoparticles and their thermal stability in the Fe-O system, *Powder Metall. Met. Ceram.*, 2021, **60**(7–8), 451–463, DOI: **10.1007/s11106-021-00256-8**.

20 B. A. Movchan, Discrete nanosized metallic coatings produced by EB-PVD, *Surf. Eng.*, 2016, **32**, 258–266, DOI: **10.1179/1743294415Y.0000000092**.

21 F. Volmer, I. Seidler, T. Bisswanger, J.-S. Tu, L. R. Schreiber, C. Stampfer and B. Beschoten, How to solve problems in micro- and nanofabrication caused by the emission of electrons and charged metal atoms during e-beam evaporation, *J. Phys. D: Appl. Phys.*, 2021, **54**, 225304, DOI: **10.1088/1361-6463/abe89b**.

22 M. Xu, A. Kumar and J. M. LeBeau, Correlating local chemical and structural order using Geographic Information Systems-based spatial statistics, *Ultramicroscopy*, 2023, **243**, 113642, DOI: **10.1016/j.ultramic.2022.113642**.

23 V. Orel, A. Shevchenko, A. Romanov, M. Tselepi, T. Mitrelias, C. H. W. Barnes, A. Burlaka, S. Lukin and I. Shchepotin, Magnetic properties and antitumor effect of nanocomplexes of iron oxide and doxorubicin, *Nanomedicine*, 2015, **11**, 47–55, DOI: **10.1016/j.nano.2014.07.007**.

24 V. E. Orel, Y. I. Kudryavets, S. Satz, N. A. Bezdenezhnih, M. L. Danko, N. N. Khranovskaya, A. V. Romanov, N. N. Dzyatkovskaya and A. P. Burlaka, Mechanochemically activated doxorubicin nanoparticles in combination with 40 MHz frequency irradiation on A-549 lung carcinoma cells, *Drug Delivery*, 2005, **12**, 171–178, DOI: **10.1080/10717540590932007**.

25 P. A. Shenoy, A. Kuo, I. Vetter and M. T. Smith, The Walker 256 breast cancer cell-induced bone pain model in rats, *Front. Pharmacol*, 2016, **7**, 286, DOI: **10.3389/fphar.2016.00286**.

26 L. A. Amaral, M. R. Santos, Y. L. V. Said, B. B. Souza, R. J. Oliveira and E. F. Santos, Walker-256 tumor: Experimental model, implantation sites and number of cells for ascitic and solid tumor development, *Braz. Arch. Biol. Technol.*, 2019, **62**, e19180284, DOI: **10.1590/1678-4324-2019180284**.

27 R. Shaw, S. Miller, J. Curwen and M. Dymond, Design, analysis and reporting of tumor models, *Lab. Anim.*, 2017, **46**, 207–211, DOI: **10.1038/laban.1257**.

28 V. E. Orel, M. Tselepi, T. Mitrelias, M. Zabolotny, M. Krotevich, A. Shevchenko, A. Rykhalskyi, A. Romanov, V. B. Orel, A. Burlaka, S. Lukin, V. Stegnii and C. H. W. Barnes, Nonlinear magnetochemical effects in nanotherapy of Walker-256 carcinosarcoma, *ACS Appl. Bio Mater.*, 2019, **2**, 3954–3963, DOI: **10.1021/acsabm.9b00526**.

29 J. A. Tayek, N. W. Istfan, C. T. Jones, K. J. Hamawy, B. R. Bistrian and G. L. Blackburn, Influence of the Walker 256 carcinosarcoma of muscle, tumor, and whole-body protein synthesis and growth rate in the cancer-bearing rat, *Cancer Res.*, 1986, **46**, 5649–5654.

30 N. Emanuel, *Kinetics of Experimental Tumor Processes*, Pergamon Press, Oxford, 1982, p. 348.

31 F. Galati, V. Rizzo, G. Moffa, C. Caramanico, E. Kripa, B. Cerbelli, G. D'Amati and F. Pediconi, Radiologic-pathologic correlation in breast cancer: do MRI biomarkers correlate with pathologic features and molecular subtypes?, *Eur. Radiol. Exp.*, 2022, **6**, 39, DOI: 10.1186/s41747-022-00289-7.

32 A. Crombé, P. J. Marcellin, X. Buy, E. Stoeckle, V. Brouste, A. Italiano, F. Le Loarer and M. Kind, Soft-tissue sarcomas: Assessment of MRI features correlating with histologic grade and patient outcome, *Radiology*, 2019, **291**, 710–721, DOI: 10.1148/radiol.2019181659.

33 E. Umut, F. Pineider, P. Arosio, C. Sangregorio, M. Corti, F. Tabak, A. Lascialfari and P. Ghigna, Magnetic, optical and relaxometric properties of organically coated gold–magnetite (Au–Fe_3O_4) hybrid nanoparticles for potential use in biomedical applications, *J. Magn. Magn. Mater.*, 2012, **324**, 2373–2379, DOI: 10.1016/j.jmmm.2012.03.005.

34 F. L. Goerner and G. D. Clarke, Measuring signal-to-noise ratio in partially parallel imaging MRI, *Med. Phys.*, 2011, **38**, 5049–5057, DOI: 10.1118/1.3618730.

35 B. Gopalakrishnan, M. Nash, M. Velayutham and F. A. Villamena, Detection of nitric oxide and superoxide radical anion by electron paramagnetic resonance spectroscopy from cells using spin traps, *J. Visualized Exp.*, 2012, **18**, e2810, DOI: 10.3791/2810.

36 L. Blumenfeld, *Problems of Biological Physics*, Springer-Verlag, Berlin, 1981, p. 224.

37 A. L. Kleschyov and M. Terekhov, Electron paramagnetic resonance in a biomedical laboratory, *Bioanalysis*, 2013, **5**, 2233–2237, DOI: 10.4155/bio.13.200.

38 A. P. Burlaka, I. I. Ganusevich, S. N. Lukin, M. R. Gafurov and E. P. Sidorik, Superoxide-and NO-dependent mechanisms of the reprogramming of bone marrow cells by tumor cells, *Appl. Magn. Reson.*, 2014, **45**, 1261–1273, DOI: 10.1007/s00723-014-0610-y.

39 Y. Ichikawa, M. Ghanefar, M. Bayeva, R. Wu, A. Khechaduri, S. V. Naga Prasad, R. K. Mutharasan, T. J. Naik and H. Ardehali, Cardiotoxicity of doxorubicin is mediated through mitochondrial iron accumulation, *J. Clin. Invest.*, 2014, **124**, 617–630, DOI: 10.1172/JCI72931.

40 M. Feygenson, J. C. Bauer, Z. Gai, C. Marques, M. C. Aronson, X. Teng, D. Su, V. Stanic, V. S. Urban, K. A. Beyer and S. Dai, Exchange bias effect in Au-Fe_3O_4 dumbbell nanoparticles induced by the charge transfer from gold, *Phys. Rev.*, 2015, **92**, 054416, DOI: 10.1103/PhysRevB.92.054416.

41 G. Brennan, S. Bergamino, M. Pescio, S. A. M. Tofail and C. Silien, The effects of a varied gold shell thickness on iron oxide nanoparticle cores in magnetic manipulation, T_1 and T_2 MRI contrasting, and magnetic hyperthermia, *Nanomaterials*, 2020, **10**, 2424, DOI: 10.3390/nano10122424.

42 A. Radoń, S. Łoński, M. Kądziołka-Gaweł, P. Gębara, M. Lis, D. Łukowiec and R. Babilas, Influence of magnetite nanoparticles surface dissolution, stabilization and functionalization by malonic acid on the catalytic activity, magnetic and electrical properties, *Colloids Surf., A*, 2020, **607**, 125446, DOI: 10.1016/j.colsurfa.2020.125446.

43 R. M. Lubken, A. M. de Jong and M. W. J. Prins, How reactivity variability of biofunctionalized particles is determined by superpositional heterogeneities, *ACS Nano*, 2021, **15**, 1331–1341, DOI: 10.1021/acsnano.0c08578.

44 V. E. Orel, N. O. Bezdenezhnykh, M. O. Nikolov, A. V. Romanov, N. M. Khranovskaya, O. V. Skachkova, Yu. I. Kudryavets and I. B. Schepotin, Comparative study of antitumor effect Fe_2O_3 and Fe_3O_4 nanoparticles in nanocomplex with doxorubicin during electromagnetic irradiation and modification of human hepatocellular carcinoma cells (HepG2) with interferon-alpha, *Clin. Oncol.*, 2013, **1**, 141–144.

45 Y. Xing, U. Jin, J. Si, M. Peng, X. Wang, C. Chen and Y. Cui, Controllable synthesis and characterization of Fe_3O_4/Au composite nanoparticles, *J. Magn. Magn. Mater.*, 2015, **380**, 150–156, DOI: 10.1016/j.jmmm.2014.09.060.

46 J. Canet-Ferrer, P. Albella, A. Ribera, J. V. Usagrea and S. A. Maiera, Hybrid magnetite-gold nanoparticles as bifunctional magnetic-plasmonic systems: three representative cases, *Nanoscale Horiz.*, 2017, **2**, 205–216, DOI: 10.1039/c6nh00225k.

47 N. Spaldin, Ferromagnetic domains, in *Magnetic Materials: Fundamentals and Applications*, Cambridge University Press, 2010, pp. 79–95, DOI: 10.1017/CBO9780511781599.007.

48 E. H. Frei, S. Shtrikman and D. Treves, The bistable behaviour of the magnetic transductor, *Phys. Rev.*, 1956, **106**, 446–455, DOI: 10.1088/0508-3443/9/10/304.

49 D. L. Leslie-Pelecky and R. D. Rieke, Magnetic properties of nanostructures materials, *Chem. Mater.*, 1996, **8**, 1770–1783, DOI: 10.1021/cm960077f.

50 S. Gangopadhyay, G. C. Hadjipanayis, B. Dale, C. M. Sorensen, K. J. Klabunde, V. Papaefthymiou and A. Kostikas, Magnetic properties of ultrafine iron particles, *Phys. Rev. B: Condens. Matter Mater. Phys.*, 1992, **45**, 9778–9787, DOI: 10.1103/physrevb.45.9778.

51 V. R. R. Aquino, L. C. Figueiredo, J. A. H. Coaquira, M. H. Sousa and A. F. Bakuzis, Magnetic interaction and anisotropy axes arrangement in nanoparticle aggregates can enhance or reduce the effective magnetic anisotropy, *J. Magn. Magn. Mater.*, 2020, **498**, 166170, DOI: 10.1016/j.jmmm.2019.166170.

52 G. G. Martins, F. A. Lívero, A. M. Stolf, C. M. Kopruszinski, C. C. Cardoso, O. C. Beltrame, J. E. Queiroz-Telles, R. L. Strapasson, M. E. Stefanello, R. Oude-Elferink and A. Acco, Sesquiterpene lactones of Moquiniastrum polymorphum subsp. floccosum have antineoplastic effects in Walker-256 tumor-bearing rats, *Chem.-Biol. Interact.*, 2015, **228**, 46–56, DOI: 10.1016/j.cbi.2015.01.018.

53 S. Revannasiddaiah, V. V. Maka and S. K. Devadas, Tumour growth kinetics as a potential predictive and prognostic

factor in carcinoma of the lung, *Ann. Transl. Med.*, 2019, **7**, 295, DOI: 10.21037/atm.2019.07.39.

54 J. Gautier, E. Allard-Vannier, E. Munnier, M. Souce and I. Chourpa, Recent advances in theranostic nanocarriers of doxorubicin based on iron oxide and gold nanoparticles, *J. Controlled Release*, 2013, **169**, 48–61, DOI: 10.1016/j.jconrel.2013.03.018.

55 X. Chao, F. Shi, Y. Y. Zhao, K. Li, M. L. Peng, C. Chen and Y. L. Cui, Cytotoxicity of Fe_3O_4/Au composite nanoparticles loaded with doxorubicin combined with magnetic field, *Pharmazie*, 2010, **65**, 500–504.

56 I. Venugopal, S. Pernal, A. Duproz, J. Bentley, H. Engelhard and A. Linninger, Magnetic field-enhanced cellular uptake of doxorubicin loaded magnetic nanoparticles for tumor treatment, *Mater. Res. Express*, 2016, **3**, 095010, DOI: 10.1088/2053-1591/3/9/095010.

57 J. Gold, Inhibition of Walker 256 intramuscular carcinoma in rats by administration of hydrazine sulfate, *Oncology*, 1971, **25**, 66–71, DOI: 10.1159/000224555.

58 E. L. Lushnikova, E. V. Ovsyanko, L. M. Nepomnyashchikh, A. V. Efremov and D. V. Morozov, Proliferation of Walker 256 carcinosarcoma cells: effect of whole-body hyperthermia and antitumor agents, *Bull. Exp. Biol. Med.*, 2011, **152**, 146–152, DOI: 10.1007/s10517-011-1475-9.

59 J. M. Tse, G. Cheng, J. A. Tyrrell, S. A. Wilcox-Adelman, Y. Boucher, R. K. Jain and L. L. Munn, Mechanical compression drives cancer cells toward invasive phenotype, *Proc. Natl. Acad. Sci. U. S. A.*, 2012, **109**, 911–916, DOI: 10.1073/pnas.1118910109.

60 Y. Qiu, S. Tong, L. Zhang, Y. Sakurai, D. R. Myers, L. Hong, W. A. Lam and G. Bao, Magnetic forces enable controlled drug delivery by disrupting endothelial cell-cell junctions, *Nat. Commun.*, 2017, **8**, 15594, DOI: 10.1038/ncomms15594.

61 F. Davnall, C. S. Yip, G. Ljungqvist, M. Selmi, F. Ng, B. Sanghera, B. Ganeshan, K. A. Miles, G. J. Cook and V. Goh, Assessment of tumor heterogeneity: an emerging imaging tool for clinical practice?, *Insights Imaging*, 2012, **3**, 573–589, DOI: 10.1007/s13244-012-0196-6.

62 M. V. Efremova, V. A. Naumenko, M. Spasova, A. S. Garanina, M. A. Abakumov, A. D. Blokhina, P. A. Melnikov, A. O. Prelovskaya, M. Heidelmann, Z. A. Li, Z. Ma, I. V. Shchetinin, Y. I. Golovin, I. I. Kireev, A. G. Savchenko, V. P. Chekhonin, N. L. Klyachko, M. Farle, A. G. Majouga and U. Wiedwald, Magnetite-Gold nanohybrids as ideal all-in-one platforms for theranostics, *Sci. Rep.*, 2018, **8**, 11295, DOI: 10.1038/s41598-018-29618-w.

63 Y. Ikeda, J. H. Anderson and D. M. Long, Oxygen free radicals in the genesis of traumatic and peritumoral brain edema, *Neurosurgery*, 1989, **24**, 679–685, DOI: 10.1227/00006123-198905000-00004.

64 L. Morbidelli, S. Donnini and M. Ziche, Role of nitric oxide in tumor angiogenesis, *Cancer Treat. Res.*, 2004, **117**, 155–167, DOI: 10.1007/978-1-4419-8871-3_11.

65 W. Dröge, Free radicals in the physiological control of cell function, *Physiol. Rev.*, 2002, **82**, 47–95, DOI: 10.1152/physrev.00018.2001.

66 M. V. Clément and S. Pervaiz, Intracellular superoxide and hydrogen peroxide concentrations: a critical balance that determines survival or death, *Redox Rep.*, 2001, **6**, 211–214, DOI: 10.1179/135100001101536346.

67 M. P. Murphy, Nitric oxide and cell death, *Biochim. Biophys. Acta*, 1999, **1411**, 401–414, DOI: 10.1016/s0005-2728(99)00029-8.

68 L. P. Michaelson, C. Iler and C. W. Ward, ROS and RNS signaling in skeletal muscle: critical signals and therapeutic targets, *Annu. Rev. Nurs. Res.*, 2013, **31**, 367–387, DOI: 10.1891/0739-6686.31.367.

69 C. K. Sen and S. Roy, Redox signals in wound healing, *Biochim. Biophys. Acta*, 2008, **1780**, 1348–1361, DOI: 10.1016/j.bbagen.2008.01.006.

70 J. M. Kembro, S. Cortassa, D. Lloyd, S. J. Sollott and M. A. Aon, Mitochondrial chaotic dynamics: Redox-energetic behavior at the edge of stability, *Sci. Rep.*, 2018, **8**, 15422, DOI: 10.1038/s41598-018-33582-w.

71 J. Schreiber, C. Mottley, B. K. Sinha, B. Kalyanaraman and R. P. Mason, One-electron reduction of daunomycin, daunomycinone, and 7-deoxydaunomycine by the xanthine xanthine-oxidase system - Detection of semiquinone free-radicals by electron-spin-resonance, *J. Am. Chem. Soc.*, 1987, **109**, 348–351, DOI: 10.1021/ja00236a009.

72 B. Kalyanaraman, E. Perez-Reye and R. P. Mason, Spin-trapping and direct electron spin resonance investigations of the redox metabolism of quinone anticancer drugs, *Biochim. Biophys. Acta*, 1980, **630**, 119–130, DOI: 10.1016/0304-4165(80)90142-7.

73 G. Ferrer-Sueta and R. Radi, Chemical biology of peroxynitrite: kinetics, diffusion, and radicals, *ACS Chem. Biol.*, 2009, **4**, 161–177, DOI: 10.1021/cb800279q.

74 B. Greenebaum and F. Barnes, *Biological and Medical Aspects of Electromagnetic Fields*, CRC Press, 2018, DOI: 10.1201/9781315186641.

75 S. Tofani, D. Barone, M. Cintorino, M. M. de Santi, A. Ferrara, R. Orlassino, P. Ossola, F. Peroglio, K. Rolfo and F. Ronchetto, Static and ELF magnetic fields induce tumor growth inhibition and apoptosis, *Bioelectromagnetics*, 2001, **22**, 419–428, DOI: 10.1002/bem.69.

76 V. E. Orel, M. Tselepi, T. Mitrelias, A. Rykhalskyi, A. Romanov, V. B. Orel, A. Shevchenko, A. Burlaka, S. Lukin and C. H. W. Barnes, Nanomagnetic modulation of tumor redox state, *Nanomedicine*, 2018, **14**, 1249–1256, DOI: 10.1016/j.nano.2018.03.002.

77 V. Makrin and I. Vagner, Clinical hyperthermia by resonant selective tumor destruction tuned by hyperfine interaction: I. Basic model, *HIT J. Sci. Eng. A.*, 2006, **3**(1), 162–168.

78 A. Sharma, U. Sharma, N. R. Jagannathan, R. Ray and M. R. Rajeswari, Effect of doxorubicin on squamous cell carcinoma of skin: Assessment by MRI relaxometry at 4.7T, *Cancer Invest.*, 2019, **37**, 339–354, DOI: 10.1080/07357907.2019.1651327.

79 R. W. Tain, A. M. Scotti, W. Li, X. J. Zhou and K. Cai, Imaging short-lived reactive oxygen species (ROS) with endogenous contrast MRI, *J. Magn. Reson. Imaging*, 2018, **47**, 222–229, DOI: 10.1002/jmri.25763.